# UNIVERSITYOF BIRMINGHAM

# A self-tuned rotational vibration energy harvester for self-powered wireless sensing in powertrains

Gunn, B.; Alevras, P.; Flint, J. A.; Fu, H.; Rothberg, S. J.; Theodossiades, S.

[Link to publication on Research at Birmingham portal](Link to publication on Research at Birmingham portal)

# A self-tuned rotational vibration energy harvester for self-powered wireless sensing in powertrains

B. Gunn [a], P. Alevras [b], J.A. Flint [a], H. Fu [a], S.J. Rothberg [a], S. Theodossiades [a],[*]

[a] *Wolfson School of Mechanical, Electrical and Manufacturing Engineering, Loughborough University, Loughborough LE11 3TU, UK*
[b] *Department of Mechanical Engineering, School of Engineering, University of Birmingham, Edgbaston, Birmingham B15 2TT, UK*

## HIGHLIGHTS

- Novel self-tuning rotational vibration energy harvester concept for powertrains.
- The concept eliminates the use of protruding beams in rotational vibration energy harvester.
- Pendulum on tautochrone path for resonance matching a rotational frequency order.
- The generated power drives an electronic circuit with a temperature sensor.
- A physical prototype tested at lab validates the proposed design.

## ARTICLE INFO

## ABSTRACT

During conversion between mechanical and electrical energy within a machine, or vice-versa, vibrations (or perturbations of the rotational speed) are usually present. These vibrations can be converted into relatively small but useful amounts of electrical energy that can power wireless sensors. In this paper, a novel self-tuning concept of a rotational vibration energy harvester for energy conversion applications is presented. The design concept combines a self-tuned oscillator with an eccentric mass on a "tautochrone" path of motion so that its natural frequency matches a selected order of the rotational speed of a powertrain in order to harness the energy of rotational oscillations. This original vibration energy harvester design (which does not require protruding beams) enables the implementation of the concept for propulsion applications with the appropriate tuning condition. The mathematical modelling of the device and selection of the key design parameters suggest sufficient generated power to successfully drive an electronic circuit equipped with a temperature sensor. A physical prototype is manufactured and experimentally tested, validating the proposed design. The device is demonstrated to be capable of powering a wireless temperature sensor transmitting data every 2 s for a range of more than 1000 rpm of the shaft rotational speed. Higher data transmission rates could be achieved by optimising the design of the harvester, which currently has an overall volume <60 cm$^3$.

## 1. Introduction

During the process of converting between electrical and mechanical power within a machine, unwanted energy is usually manifested in the form of mechanical oscillations. Whilst this surplus energy is relatively small compared with the energy being converted, it can be useful for powering sensors and other low-power electronic devices. Furthermore, this energy is present in locations deep inside the machine which may be difficult to reach with wires and when paired with a suitable radio can form the basis of a fully integrated wireless self-powering sensor. The potential applications for such a device are extensive and range from generators such as wind turbines [1], and powertrains [2] found in internal combustion engines and electric motors. By enabling this type of wireless monitoring, challenging monitoring tasks can be achieved in difficult to reach areas within the machine, allowing parameters such as temperature, forcing, fluid properties etc. to be measured. As a result, the machine's health can be monitored in a much more detailed way, reducing maintenance and down-time while enabling operation to be optimised. The present paper focuses on a novel energy harvesting device that can be mounted on a rotating shaft, and which is highly
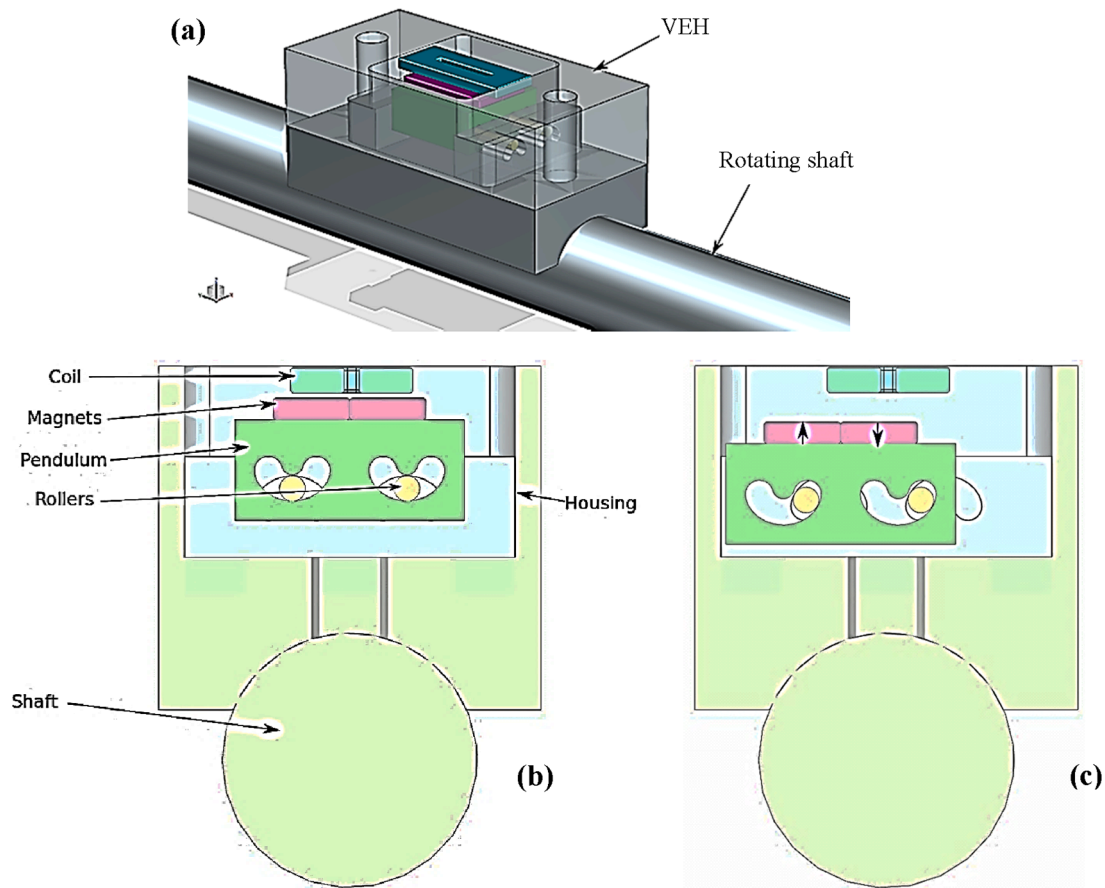
**Fig. 1.** (a) Schematic of the pendulum VEH device and (b), (c) two relative positions of the VEH magnets and coils during operation.

applicable to rotating machines. During operation, these devices change their vibrational conditions according to the load (both electrical and mechanical) and rotational speed. This wide range of operating conditions is a challenge that needs to be addressed in the design of the harvester and will be considered in the present work.

Vibration Energy Harvesters (VEH) have already found a wide range of applications in control and structural health monitoring systems [3,4]. Three main VEH technologies have dominated: piezoelectric, electromagnetic and electrostatic. In general, piezoelectric and electrostatic are better suited to small, low power Micro Electro-Mechanical Systems (MEMS) applications [5], whereas electromagnetic energy harvesters are predominantly used in larger ($> 0.5$ cm$^3$) applications, where more power is required [6,7].

VEH is most effective at or near resonance operating conditions, which has prompted researchers to investigate methods for broadening the useful frequency range of VEH due to the broadband operating conditions of engineering systems [8]. Tyre pressure monitoring systems have attracted particular interest from a rotating VEH design perspective. Several piezoelectric VEH systems have been developed, employing cantilever beams with increasing stiffness as the centripetal force increases along with the wheel speed [9,10]. For electromagnetic VEH that harness energy from rotating components, pendulums have been used to ensure resonance is achieved at a wide shaft speed range [11]. Maurya et al. explored the methodology of harnessing the automotive tyre deformation energy for self-powered strain sensing applications [12].

Although VEH systems have been studied extensively, there is relatively little research dedicated to VEH from rotational sources. However, this type of energy is ubiquitous in a variety of applications, ranging from offshore wind turbines to aerospace and automotive propulsion systems. Pillatsch et al. developed a frequency up-converting VEH to

harness low-frequency rotational energy sources using piezoelectric conversion and magnetic plucking [13]. Izadgoshasb et al. developed a pendulum-based VEH to covert irregular human motion into rotation in order to power wearable devices [14]. Toh et al. combined a conventional electromagnetic generator with an eccentric mass to obtain VEH using only one anchor for continuous rotational VEH [15]. Fu et al. explored the rotary-translational motion from a rolling magnet to harness ultra-low frequency energy sources from wind turbines [16].

In applications where the energy is derived from torsional oscillations of a rotating shaft, Trimble et al. [17] used a linear VEH with sufficiently broad operating range to extract energy from the random excitation of an oil rig drill. Some authors have investigated the possibility of attaching piezoelectric patches to already strained mechanical components [18,19], which has the advantage of being relatively straightforward but not necessarily suitable for applications with low strain. Gunn et al. [20] investigated the nonlinear behaviour of a magnet falling through a tube with repelling magnets at either end, which Alevras et al. [21] later found to possess rich nonlinear regimes of vibration, resulting in a broad operating speed range for VEH. Gunn et al. [22] also investigated a nonlinear duffing-type VEH which theoretically can achieve high amplitude oscillations throughout the operating range of the shaft.

As described in the aforementioned works, the key advantage of nonlinear VEH devices is their wider operating frequency (speed) range compared to their linear counterparts [23]. However, nonlinear VEH devices have the disadvantage of possessing two or more possible operating modes (with very different vibration amplitudes), which may lead to insufficient power being generated at a given time [24]. Pendulum mechanisms have the disadvantage that under high amplitude oscillation, the pendulum resonance frequency becomes nonlinear, which could lead to an undesirable low energy regime [25]. To tackle
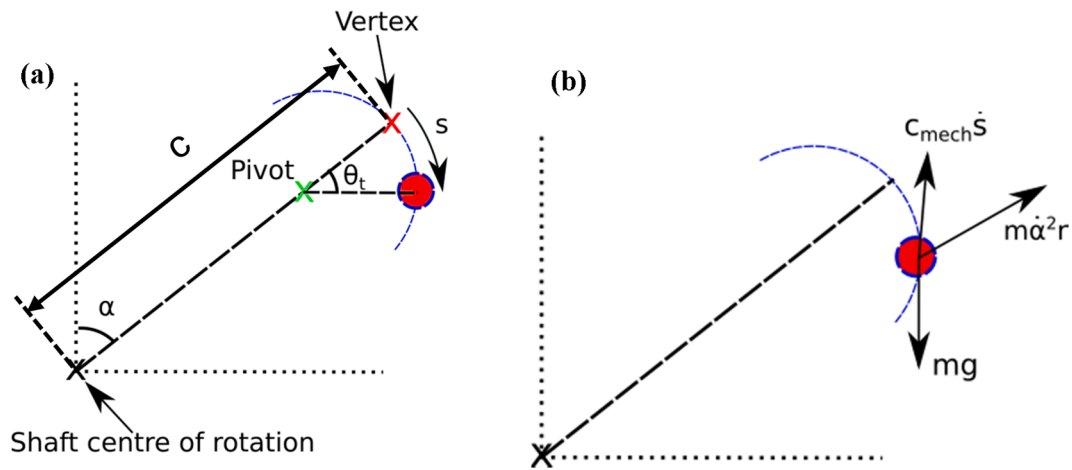
**Fig. 2.** (a) Schematic of the offset pendulum design, (b) Accompanying free body diagram.

these problems, for applications with torsional speed fluctuations (propulsion system), researchers have investigated the tuning effect of centrifugal forces on radially protruding beams. Kim [26] investigated the self-tuning piezoelectric cantilever but concluded that it was insufficient to power a sensor. Alevras et al. [27] developed a self-tuning beam energy harvester which used beams under axial preloading that interplays with the inherent rotational stiffening to ensure resonance at all operating speeds. Nevertheless, radial beams in these approaches typically require significant (radial) space when compared with the shaft diameter, whereas tuning is highly sensitive to beam thickness that may introduce durability issues.

A novel rotational VEH concept employing centrifugal pendulums is presented in this work. The mathematical modelling of the device is accompanied by manufacturing of a physical prototype and experimental validation. Unlike previous pendulum-based VEHs reported in the literature, the proposed device uses a tautochronic (epicycloid) path to ensure that resonance is achieved irrespective of the pendulum oscillation amplitude, thus eliminating the adverse effects of nonlinear behaviour due to large amplitudes of pendulum oscillations. Therefore, the pendulums can be tuned to rotational oscillations of any order (multiples of the mean rotational speed frequency) to suit different applications, which is a key novelty of this work. Furthermore, the presented pendulum-based design is compact, enabling sufficient energy amounts to be harvested across the operating range of the shaft's rotational speed. The concept fundamentally differs from other rotational VEHs presented in the literature in that no protruding beams are employed, allowing it to be installed in confined (inaccessible) spaces and mounted on shafts without introducing durability issues. This self-powered sensing system with a miniaturized self-turning rotational energy harvester provides a potential long-term solution for in-situ condition monitoring of rotating systems.

## 2. Methodology

In this section, a parametric model of a tautochronic, self-tuning VEH is developed. First, the equations of motion are adapted from the classic centrifugal pendulum absorber system described by Chao et al. [25]. A three-dimensional magnetic field model is used to calculate the electromechanical coupling factor and derive the electrical damping force acting on the pendulum VEH. Finally, the electrical power generated by the device is predicted by the model.

### 2.1. Schematic of the proposed VEH device

The proposed device consists of a bifilar pendulum mounted on a rotating shaft that is subjected to (rotational) speed fluctuations. Fig. 1

(a) shows a three-dimensional rendering of the assembled VEH mounted on the shaft. The coloured parts of the rendering indicate the VEH components, whereas the grey parts are components used to mount the VEH on the test shaft. The supporting housing is also distinguished from the VEH in Fig. 1 (b) and 1 (c). It is worth noting that the supporting structure was designed based on ease of manufacture for proof of concept purposes rather than on aiming to improve the achieved power density. The latter is a straightforward task and not part of the scope of the work herein. The VEH device comprises a bifilar pendulum that rolls on special curved tracks. The shape of the tracks is epicycloid as described by Denman [28]. Fig. 1 (b) shows the inner workings of the VEH. With the shaft extending out of the page, the steel pendulum contains the two rollers. On top of the steel block, two magnets are attached with opposing polarities as indicated by the arrows in Fig. 1 (c). A coil is attached directly on the housing above the magnets. The coil turns are wrapped around the same axis as the direction of magnetisation.

Tautochronic curved tracks are cut through the length of the pendulum, and through the housing in which they are mirrored about the axis vertical on the page. As the shaft spins, the centripetal acceleration forces the pendulum away from the centre of rotation. The pendulum is supported on the curved tracks by the rollers. As the pendulum oscillates, it is forced back to its neutral position by the centripetal acceleration which is a second order function of the shaft speed. The nature of this restoring force causes the pendulum to always be tuned to the shaft speed, thus leading to system resonance under all conditions. Fig. 1 (c) shows the assembly when the pendulum is displaced, illustrating how the pendulum and magnets move together facilitated by the rollers. The pendulum with the magnets attached moves relative to the coil attached to the housing, causing a change in the magnetic flux through the coil, which in turn induces an electromotive force in the coil.

### 2.2. Equation of motion of the VEH

Fig. 2 shows a lumped parameter model of the pendulum. In Fig. 2 (a), the centre of rotation of the shaft is labelled. The pivot point of the pendulum is fixed to the shaft and rotates about this centre. The pendulum centre of mass follows the dashed blue curved path in the diagram. The latter is shaped such that the pendulum's resonant frequency is independent of the oscillation amplitude. This epicycloid path of the pendulum motion is known as a tautochronic curve [28]. The pendulum's displacement from the vertex along its curved path is denoted by $s$ in Fig. 2 (a). The distance from the centre of rotation to the vertex of the pendulum path is denoted by $c$, whereas $\theta_t$ represents the angular displacement of the centre of mass around the pivot point.

Fig. 2 b) shows a free body diagram of the pendulum assuming the shaft is rotating with speed $\dot{\alpha}$. The centripetal acceleration is essentially acting as a restoring force, pulling the pendulum back to its vertex. As the shaft speed increases, the restoring force increases as well, affecting the resonant frequency of the pendulum in the same manner. Through appropriate design of the pendulum path, the resonant frequency can be tuned to always match a multiple order of the shaft speed [28]. In this work, the torsional speed fluctuations are of second order, so the resonant frequency is tuned to twice the shaft rotation frequency.

Chao et al. [25] have derived the equation of motion of the centrifugal pendulum vibration absorber as:

$$m\left[\ddot{s} + G(s)\ddot{\alpha} - \frac{1}{2}\frac{dX}{ds}(s)\dot{\alpha}^2\right] = -c_{mech}\dot{s} \tag{1}$$

where $c_{mech}$ is the pendulum mechanical damping, $m$ is the pendulum mass $s$ is the pendulum displacement along the arc of its path and $\alpha$ is the angular displacement of the shaft. For a standard epicycloid profile, $X(s)$ and $G(s)$ are given by:

$$X(s) = c^2 - n^2 s^2 \tag{2}$$

$$G(s) = \sqrt{c^2 - n^2(1 + n^2)s^2} \tag{3}$$

where $n$ is the tuning ratio of the pendulum.

A key assumption in the equation of motion of the pendulum VEH is that the shaft is unaffected by the pendulum motion. The assumption has been validated by numerical simulations (comprising a pendulum mass of 50 g), which showed that the oscillatory motion of the shaft was attenuated by less than 0.02%. In the works of Chao et al. [25] and Denman [28], the mass of the pendulum vibration absorber employed was significantly larger (~11.2 kg) and the action of the pendulums did reduce the shaft oscillations.

A consequence of the shaft motion being unaffected is that all pendulums move in unison since they are all excited by the same shaft speed, thus Eq. (1) applies on each pendulum. Chao et al. [25] studied the stability of the unison response and concluded that, when the following damping condition is satisfied, the unison response of the pendulums is stable throughout the feasible operating range:

$$c_{tot} \geq \frac{m^2 c^2 \Omega n}{2I_d N(1 + n^2)} \tag{4}$$

where $I_d$ is the rotor's mass moment of inertia, $\Omega$ is the rotor speed, N is the number of pendulums and $c_{tot}$ is the total damping experienced by the pendulum (mechanical and electrical). As the rotor's mass moment of inertia tends toward very large values (compared to the pendulum mass), the damping value satisfying Eq. (4) is very small.

In the works of Chao et al. [25] and Denman [28] the acceleration due to gravity was assumed to have negligible effect but, in the current application the centres of mass of the pendulums are closer to the shaft centre of rotation, making the centripetal acceleration (at low shaft rotational speeds) less significant in comparison to the gravitational acceleration. The acceleration due to gravity has a constant magnitude with direction dependent on the angle of the rotor and the position of the pendulum along its path. Denman [28] gives the tangent angle to the pendulum path as:

$$\theta_t = \frac{1}{\lambda}sin^{-1}\left(\frac{\lambda s}{\rho_0}\right) \tag{5}$$

where

$$\lambda^2 = \frac{n^2}{n^2 + 1} \tag{6}$$

and the radius of curvature at the vertex location is given by:

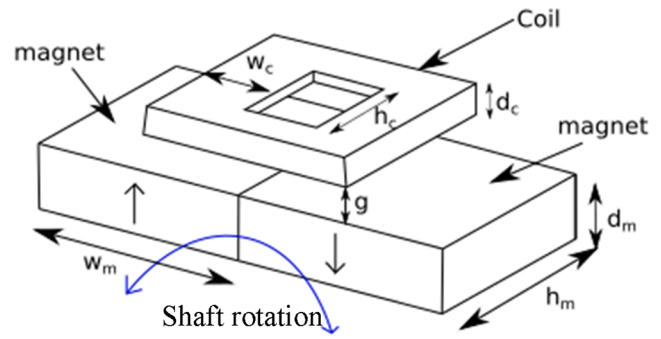$$\rho_0 \approx \frac{c}{n^2 + 1} \tag{7}$$



**Fig. 3.** Magnet and coil arrangement.

Therefore, the acceleration due to gravity along the pendulum path is given by:

$$\alpha_g = gsin(\alpha + \theta_t) \tag{8}$$

where $g$ is the acceleration due to gravity (assumed to take the value of 9.81 m/s$^2$). Adding the gravitational acceleration into the equation of motion leads to:

$$m\left[\ddot{s} + G(s)\ddot{\alpha} - \frac{1}{2}\frac{dX}{ds}(s)\dot{\alpha}^2 + gsin(\alpha + \theta_t)\right] = -c_{mech}\dot{s} \tag{9}$$

Finally, energy losses due to impacts between the pendulum and the rollers have been considered by introducing the coefficient of restitution when contact occurs [29]:

$$e = \frac{(u_b)_2 - (u_a)_2}{(u_b)_1 - (u_a)_1} \tag{10}$$

Where $u$ denotes velocity, subscripts $a$ and $b$ denote the pendulum and the roller, respectively and subscripts 1 and 2 refer to the time just before and after the impact. Due to the roller acting as an infinite barrier (having zero velocity before and after the impact), Eq. (10) simplifies to:

$$e = \frac{-(u_a)_2}{(u_a)_1} \tag{11}$$

The above condition is implemented in the numerical integration of the equation of motion when the pendulum displacement approaches the (roller) barrier (when the pendulum displacement exceeds 95% of the available path). Thus, instead of numerically integrating when impact occurs, the velocity at the next time step is calculated using Eq. (11) and the pendulum displacement is assumed to be unchanged. The coefficient of restitution was assumed to take the value 0.8 for steel-steel impacts [30].

*2.3. Electromagnetic conversion*

The pendulum VEH comprises a pair of permanent magnets with opposite polarity attached to a steel plate as shown in Fig. 1. The two magnets on the steel plate form a magnetic circuit leaving the two upper poles exposed and available to interact with the coil. It is assumed that the pendulum itself is not magnetically saturated and hence the steel can be modelled with high permeability. In such a case, the magnetic field is perpendicular to the steel surface. This can be modelled by adding an image magnet to the free space magnet to account for the steel pendulum [31]. Since the magnet interfaces directly with the steel, the effect is to double the depth of the magnet.

A rectangular coil of wire is placed near the outer face of the permanent magnets. The coil is rigidly mounted to the powertrain shaft allowing relative motion with respect to the pendulum. Due to this motion, voltage is induced in the coil as the pendulum moves back and forth. A schematic of this assembly is shown in Fig. 3 in exploded view. The coil and magnet dimensions are labelled as follows: height, depth and width are denoted by $h$, $d$ and $w$, respectively, while subscripts m
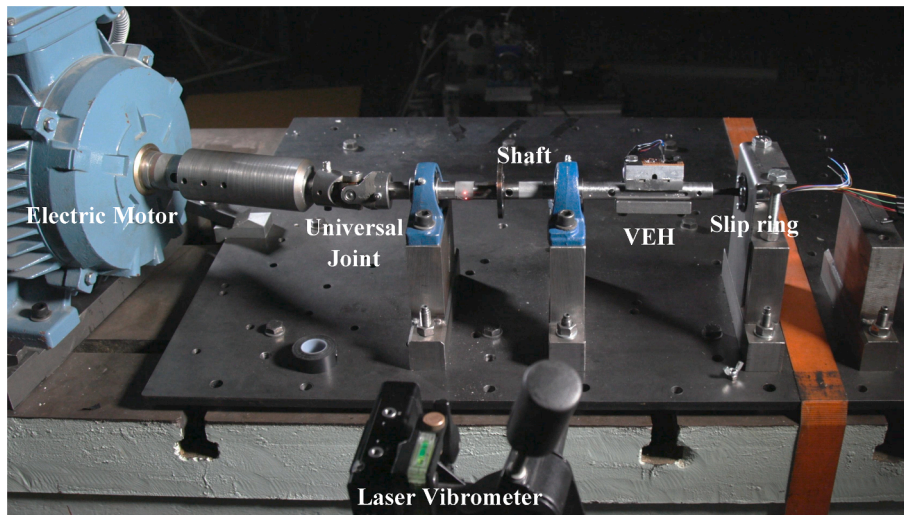
**Fig. 4.** Experimental test rig.

and c indicate magnet and coil.

The voltage $\varepsilon$ induced in the coil is given by Faraday's law:

$$\varepsilon = \widehat{\Theta}\dot{s} \tag{12}$$

where $\widehat{\Theta}$ denotes the electromagnetic coupling factor (a detailed derivation is provided in the Appendix). Correspondingly, the mechanical force acting on the pendulum due to the electrical coil is given by:

$$F_{elec} = \widehat{\Theta}I \tag{13}$$

where $I$ is the electrical current in the circuit. Assuming all power losses due to electrical interactions are transferred to the electrical circuit (no eddy current losses), the power losses in the mechanical system have to equal the power losses in the electrical circuit. Due to Ohm's law and Eq. (12), the current in the coil is given by:

$$I = \frac{\varepsilon}{R_{tot}} = \frac{\widehat{\Theta}\dot{s}}{R_{tot}} \tag{14}$$

Substituting in Eq. (13), the force acting on the pendulum is given by:

$$F_{elec} = \frac{\widehat{\Theta}^2\dot{s}}{R_{tot}} \tag{15}$$

Eq. (15) shows the electrical damping effect on the pendulum motion. It is therefore convenient to express the (viscous) electrical damping coefficient, $c_{elec}$, as:

$$c_{elec} = \frac{\widehat{\Theta}^2}{R_{tot}} \tag{16}$$

Thus, the power in the electric circuit is given by:

$$P = I^2 R_{tot} = \frac{(\widehat{\Theta}\dot{s})^2}{R_{tot}} \tag{17}$$

which can be simplified by substitution of Eq. (16) to give:

$$P = c_{elec}\dot{s}^2 \tag{18}$$

Then the power dissipated in the load resistor (usable power) is given by:

$$P_{load} = P\frac{R_{load}}{R_{int} + R_{load}} = \frac{c_{elec}\dot{s}^2 R_{load}}{R_{int} + R_{load}} \tag{19}$$

When the electrical damping term is incorporated in the equation of motion, it becomes:

$$m\left[\ddot{s} + G(s)\ddot{\alpha} - \frac{1}{2}\frac{dX}{ds}(s)\dot{\alpha}^2 + g\sin(\alpha + \theta_t)\right] = -(c_{mech} + c_{elec})\dot{s} \tag{20}$$

Eq. (20) can be used to calculate the dynamic response of the pendulum VEH and equation (19) then gives the usable electrical power.

## 3. Experimental set up

This section describes the experimental setup of the proposed VEH and the manufactured prototype. Experimental measurements have been obtained to characterise the system. The test rig where the VEH is mounted utilises a universal joint to instigate rotational speed fluctuations in a rotating shaft. The VEH is tested in open circuit to verify that the motion of the pendulum can be accurately predicted by the numerical model. Electrical load resistors are then added to validate the electromechanical interactions and the power generated. Finally, a temperature sensor is connected to the VEH via a microcontroller with wireless transmitter (as the load) to complete the proof of concept.
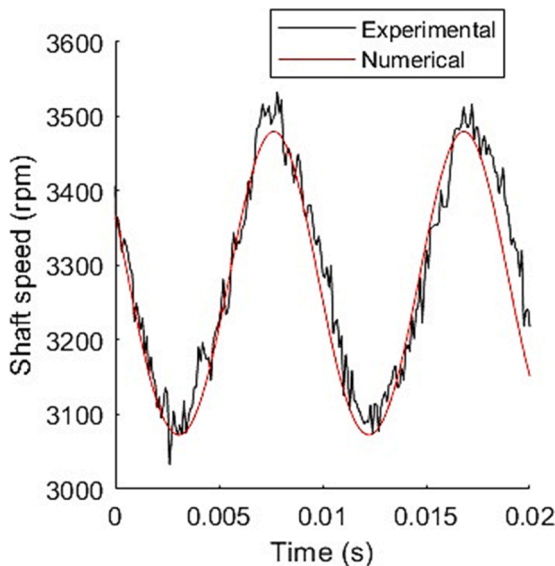


**Fig. 5.** Comparison between numerically predicted and experimentally measured shaft speed.
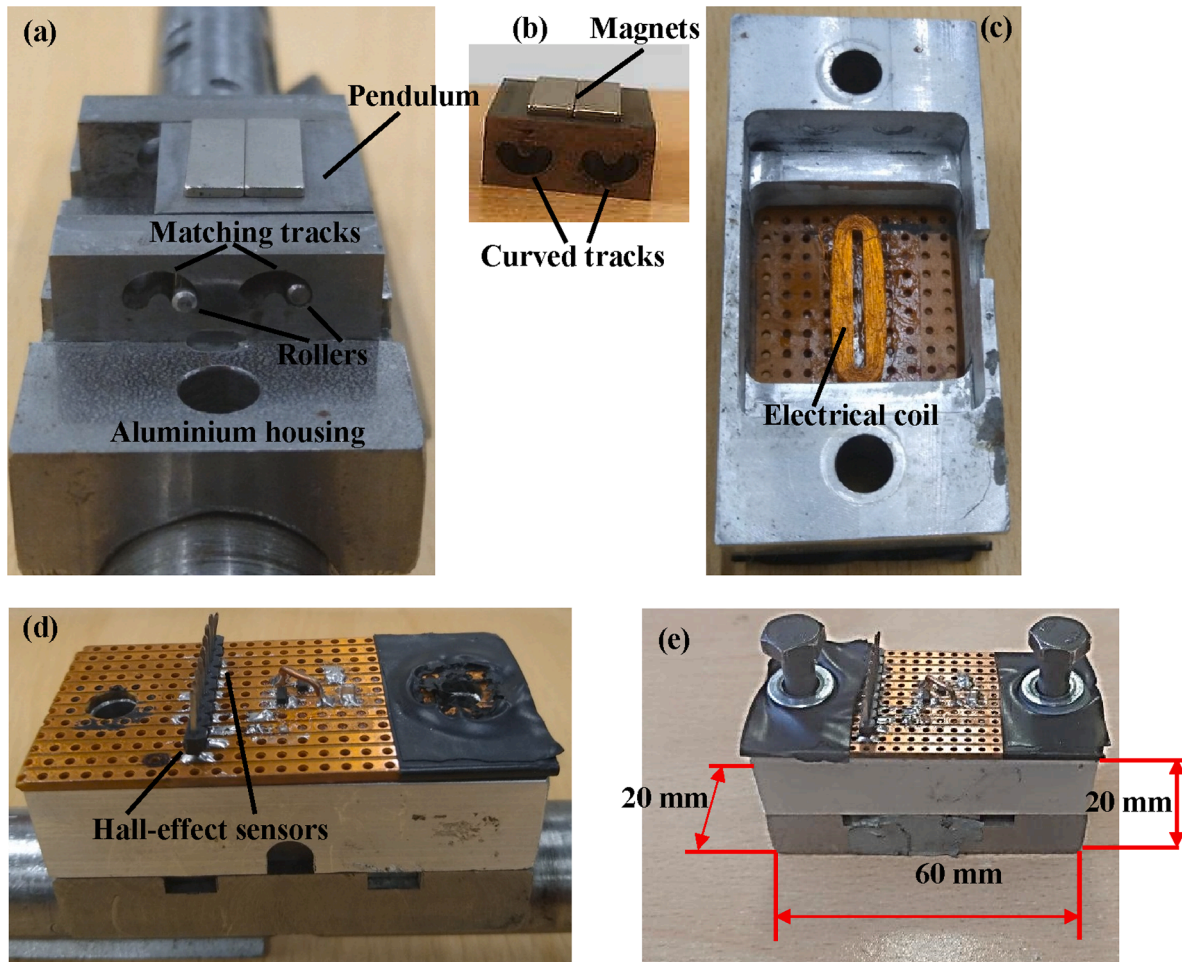
**Fig. 6.** The pendulum VEH prototype.

### 3.1. Powertrain test rig

Fig. 4 shows the rig used to test the VEH prototype. A 4-pole, 3-phase electric motor (maximum power 11 kW and 0.06543 kg·m$^2$ inertia) is connected to an unloaded shaft via a universal joint. The universal joint introduces second order oscillations in the shaft when the motor runs at constant speed. The VEH is attached to the unloaded shaft and harnesses energy from the rotational speed fluctuations. A two-beam laser vibrometer is used to measure the angular velocity of the shaft. A slip ring is used to measure the voltage generated by the VEH and ultimately

**Table 1**
Parameters of the physical prototype.

| Parameter | Value |
|---|---|
| Tuning order, $n$ | 2 |
| Pendulum radial offset, $c$ | 24 mm |
| Pendulum mass, $m_p$ | 21.6 g |
| Magnet height | 15 mm |
| Magnet depth | 2 mm |
| Magnet width | 5 mm |
| Air gap | 0.5 mm |
| Coil inner width | 1.5 mm |
| Coil outer width | 6 mm |
| Coil inner height | 18 mm |
| Coil depth | 2 mm |
| Wire diameter | 63 μm |
| Number of coil turns | 620 |
| Internal resistance | 154 Ω |
| Mechanical damping, $\zeta_{mech}$ | 1.3% |

connects the latter to the micro-controller.

The shaft oscillations are predicted using the rotational speed condition at the universal joint [32]:

$$\dot{\alpha} = \dot{\alpha}_m \frac{cos(\gamma)}{1 - sin^2(\gamma) - sin^2(\gamma)a_m} \tag{21}$$

where $\alpha_m$ denotes the angular position of the electric motor output shaft and $\gamma$ is the angle between the universal joint centrelines. Differentiation of the above provides the shaft acceleration:

$$\ddot{\alpha} = \frac{\ddot{\alpha}_m cos(\gamma)}{1 - sin^2(\gamma) - cos^2(a_m)} - \dot{a}_m^2 \frac{cos(\gamma)sin^2(\gamma)sin(2a_m)}{\left(1 - sin^2(\gamma)sin^2(a_m)\right)^2} \tag{22}$$

The angle $\gamma$ of the universal joint can be adjusted by moving the motor. When $\gamma = 10°$, the predicted angular velocity of the shaft is shown in Fig. 5, compared to the experimentally measured shaft speed with the VEH mounted. Although some noise is noted due to the laser equipment, the results validate Eq. (21). The shaft rotation is approximately sinusoidal around a mean speed value.

### 3.2. Prototype VEH

Fig. 6 shows the manufactured prototype VEH. In the middle of the VEH (Fig. 6 (a) and inset of Fig. 6 (b)), a steel block with magnets attached on one side is acting as the pendulum. Through the length of this block, specially shaped curved tracks (Fig. 6 (b)) have been cut using a wire erosion method. Steel rollers with 2 mm diameter run through the pendulum centre and into matching tracks on either side of the VEH. The aluminium housing (Fig. 6 (a)) accommodates the retaining bolts,
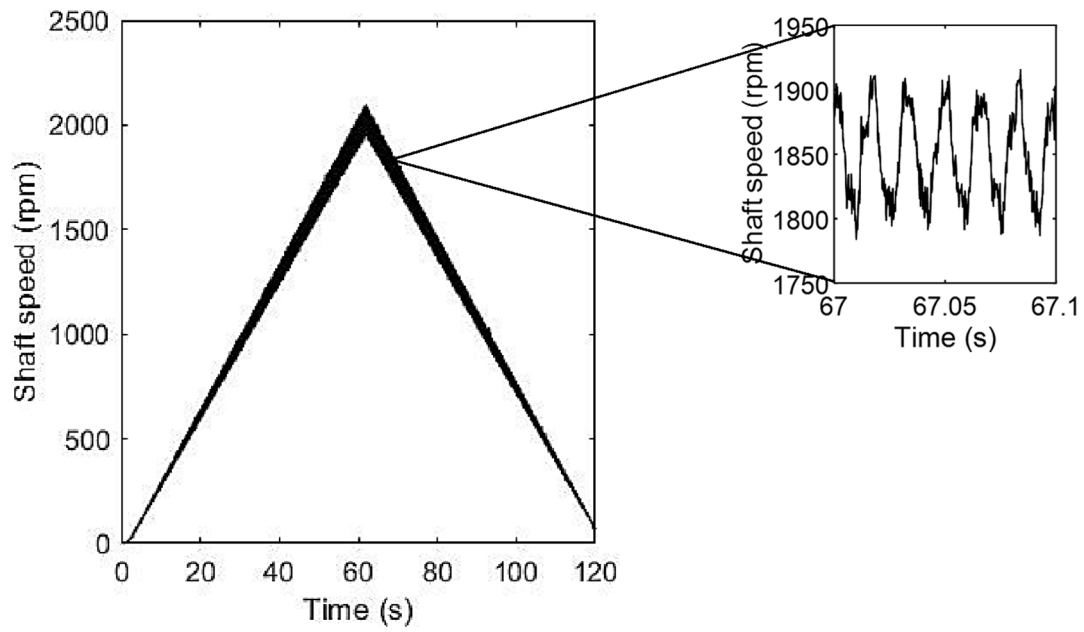
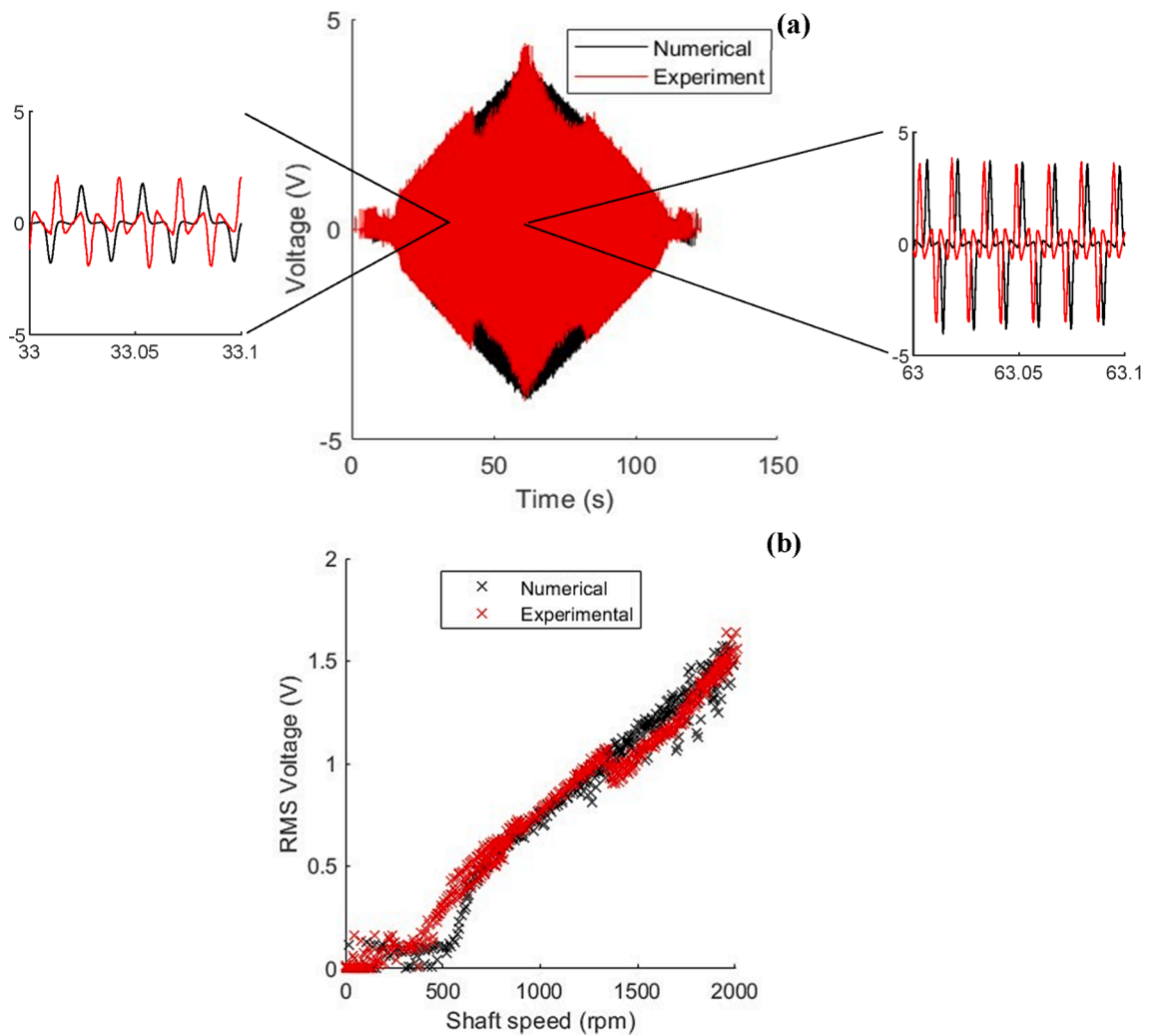**Fig. 7.** Shaft speed sweep time history.



**Fig. 8.** Comparison between experimentally measured voltage and numerical predictions (a) time history results, (b) rms voltage against shaft speed.
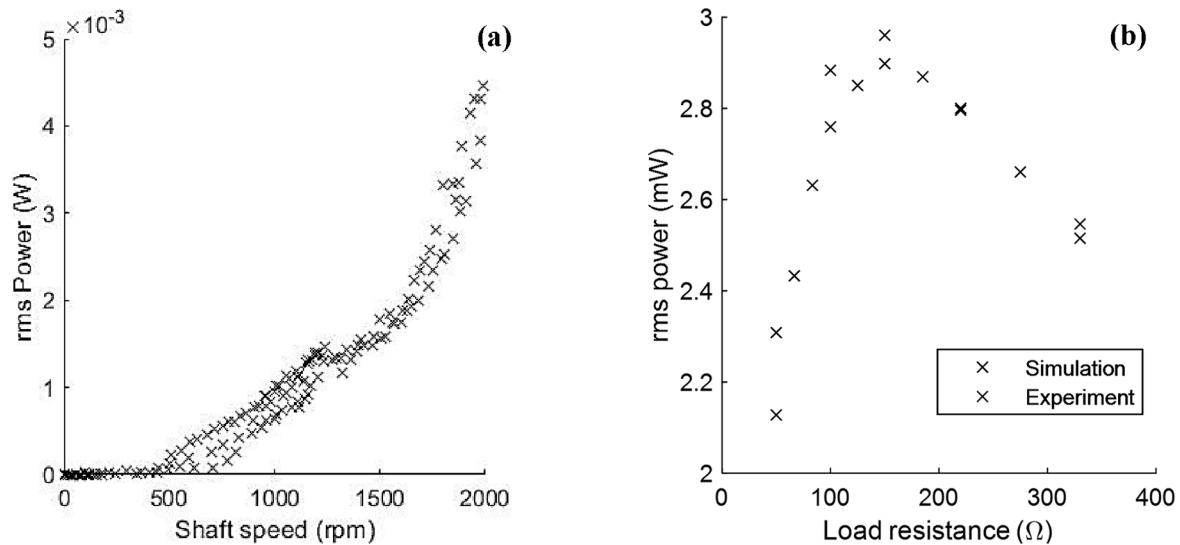
**Fig. 9.** VEH rms power with respect to (a) shaft speed (for 150 Ω load) and (b) load resistance.

preventing the rollers from sliding out of their grooves during operation. Aluminium was used because it does not have ferromagnetic properties (thus, it will not attract the magnets, affecting the system dynamics). Fig. 6 (c) shows a perforated circuit board with an air-cored electrical coil glued in the middle. On the top side of the board shown in Fig. 6 (d), two Hall-effect sensors are mounted to determine the position of the pendulum. The fully assembled VEH is shown in Fig. 6 (e). The overall envelope of the device measures 62 × 30 × 28 mm. However, the length can be reduced by applying a more elegant means of clamping the device to the shaft (removing the need to have bolts on either side of the harvester).

The pendulum is made of steel because, as described in section 2.3, its ferromagnetic properties effectively double the depth of the magnet. The aluminium housing could suffer from eddy current losses, which would effectively dampen the pendulum motion, reducing the power output. However, the housing is sufficiently far from the magnets for this effect to be negligible. Table 1 shows a summary of key parameters of the VEH physical prototype. Other parameters such as mechanical damping will be explored in more detail in the subsequent sections. Table 1 also provides the key magnet and coil dimensions. The magnets are made of N42 grade Neodymium.

## 4. Experimental results of the VEH prototype

In this section, the performance of the VEH will be assessed and compared to the numerical predictions. First, the VEH is run open-circuit to establish the pendulum uncoupled motion and then electrical load resistors are added to assess power generation. Finally, a wireless temperature sensing unit equipped with a microcontroller is connected to the VEH to assess data transmission capabilities of the end-to-end self-powered wireless sensing system.

### 4.1. Open circuit test

In this experiment, the motor is set at 15° with respect to the driven shaft on which the VEH is mounted. The motor speed is accelerated from rest to 2000 rpm in 60 s, then back to rest in another 60 s. The measured shaft speed throughout this manoeuvre is shown in Fig. 7. It can be noted that as the shaft speed increases, the amplitude of oscillations increases (as shown in the inset of the figure).

During the experiment, the shaft speed was measured using a laser beam vibrometer and the voltage was measured from the coil of the VEH. Fig. 8 shows the generated voltage throughout the manoeuvre. The

numerical model used the measured shaft speed as input and all other parameters took the values shown in Table 1. The mechanical damping ratio is configured to a constant value to match the open circuit voltage results (it is widely accepted that maximum power can be obtained when the mechanical damping is equal to electrical damping). In Fig. 8 (b), the rms voltage is plotted against speed for one complete cycle in every 100 cycles of oscillatory motion. The figure shows excellent correlation between the numerical and experimental results. No hysteresis can be observed between the accelerating and decelerating sweeps, indicating that the pendulum VEH exhibits at most only weak nonlinearities. Below 500 rpm, the acceleration due to gravity is more significant than the centripetal acceleration, thus the only voltage generated here is a consequence of the pendulum falling from one side to the other (within its path of motion) as gravity dictates. Above 500 rpm, the rms voltage increases linearly with shaft speed. At around 1300 rpm, the experimental results deviate slightly from the numerical model. This coincides with an audible clattering noise when running the rig, which could indicate severe pendulum impacts.

### 4.2. Electrical load resistance

In this experiment, the test rig was set up in the same way as in the sweep test described in Section 4.1. Load resistors were connected one at a time between the coil terminal and the voltage drop was measured. The load resistance was changed in steps through 50 Ω, 100 Ω, 150 Ω, 220 Ω and 330 Ω. The forward–backward speed sweep was repeated for each resistor. Fig. 9 (a) shows the rms power plotted against shaft speed for the 150 Ω load resistor. As expected, the power output increases with shaft speed. At 2000 rpm the rms power reaches 4.5 mW, generating an amount of power throughout the manoeuvre from around 1 mW as early as 1100 rpm.

Fig. 9 (b) shows the rms power generated throughout the full manoeuvre for each electrical load resistance. The maximum power is found when the load resistance matches the internal resistance of the coil (154 Ω). Numerical integration of the equation of motion was repeated at each load resistance and shows agreement with experimental results to within 10%. The significance of these results is to validate the electromechanical model of the VEH. With a passive resistive load, the power generated follows the expected power output to within 10% over the full drive cycle. This allows for the design of a VEH based on the procedure outlined in Section 3 and a confident prediction of its power output.
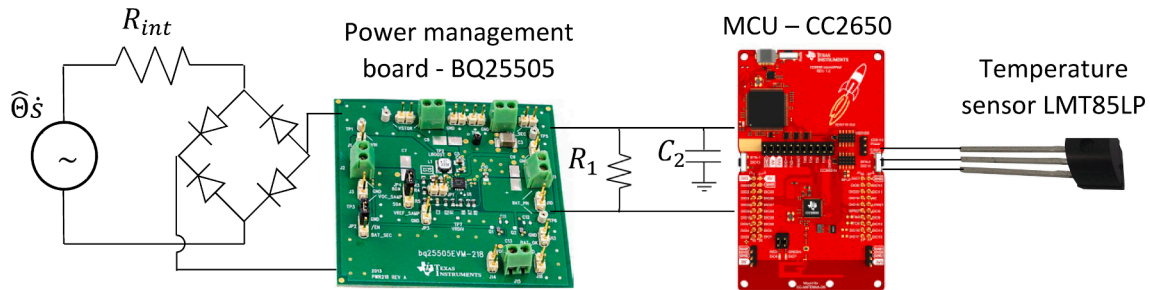
**Fig. 10.** Schematic diagram of the VEH circuit. From left to right, the coil of the device is connected to a bridge rectifier, with voltage output connected to the power management board. The board supplies voltage to the energy storage capacitor ($C_2$) that is connected to the microcontroller (MCU). The temperature sensor is controlled by the MCU that collects data when the capacitor $C_2$ is charged and transmits it wirelessly.
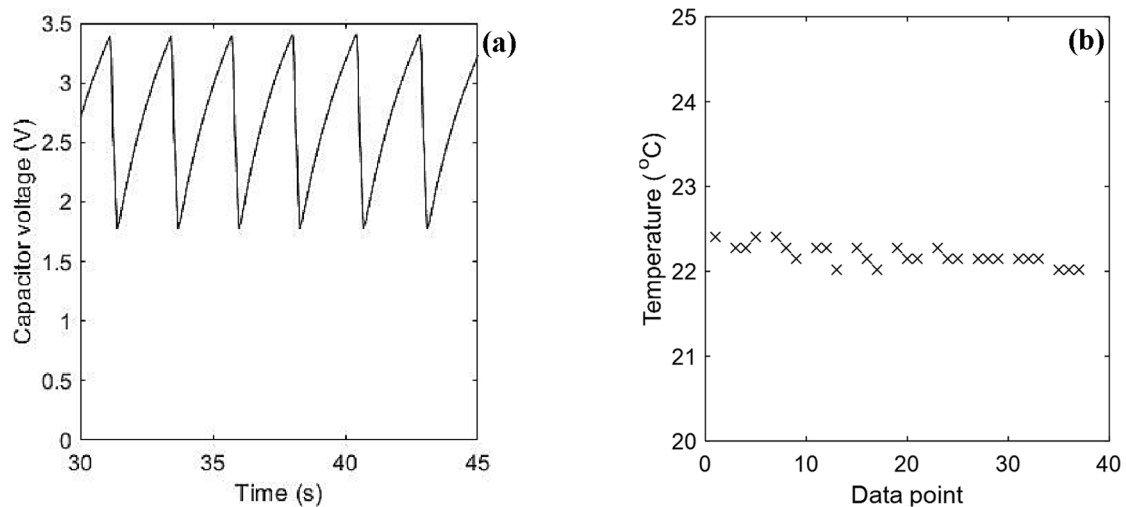


**Fig. 11.** (a) Data transmission cycles at 2000 rpm and (b) Measured temperature data.

### 4.3. Powering a wireless sensor

The VEH has been characterised with passive load resistors to determine AC power generation but most sensor circuits need a continuous voltage DC supply and hence experiments were conducted to assess this situation. Hereafter, a microcontroller with built-in wireless radio is connected to the VEH via a diode bridge rectifier and a power management integrated circuit (IC). The microcontroller measures the voltage across a temperature sensor and transmits it wirelessly to another microcontroller which is connected to a PC to capture the data.

Fig. 10 shows a schematic representation of the test. The VEH is connected to a Schottky diode bridge rectifier. The DC output is then fed into a BQ25505 power management board, which charges a 330 μF capacitor ($C_2$) that is connected to a Texas Instruments CC2650 Launchpad. The BQ25505 board triggers an output signal, which controls the reset mode of the CC2650 microcontroller. When the capacitor $C_2$ is charged to 3.3 V, the CC2650 turns on and runs a program which reads the voltage of the temperature sensor through its analogue input and transmits it to a wireless receiver. When the voltage across the capacitor drops below 1.8 V, the CC2650 goes into reset mode and the capacitor is then able to recharge. The cycle repeats with data transmission occurring whenever the capacitor is sufficiently charged. Entering a reset mode each time and using this strategy ensures that the microcontroller always starts in a known state and that there is adequate stored energy to complete the monitoring and transmit cycle.

Three tests were carried out with the motor running at constant speeds of 1200, 1500 and 2000 rpm. Below 1200 rpm, insufficient power was generated to reliably power the microcontroller. Fig. 11 (a) shows the capacitor voltage charging and discharging phases through

several transmission cycles at 2000 rpm. As the capacitor charges, the microcontroller is in reset mode and draws negligible current (0.1 μA, [33]). The capacitor takes 2 s to charge and discharges in 0.3 s. Less power is generated at lower speeds. The charge times at 1500 and 1200 rpm are 4.7 s and 11 s, respectively.

The microcontroller reads the sensor output at 200 Hz and transmits the measured voltage wirelessly to a receiver, which sends the data to a laptop personal computer (PC), where it is converted to temperature reading (shown in Fig. 11 (b)). The temperature in the lab was measured using a thermocouple and was found to be 22 °C. In this sample application, three data packets were transmitted before the microcontroller was turned off. Each packet contained 7 bytes of data, four of which were the temperature data. Ultimately the sensor that can be used in a final application might not need to transmit data continuously e.g. if data is only required at specific time intervals. Then, with a suitably sized capacitor, higher data transmission rates could be used. However, longer recharge times will be necessary. Taking into account that temperature sensing generally has low power requirements with low sampling rates compared to other measurements, this demonstration shows that the achieved power density is more than adequate to wirelessly cover the power requirements of temperature measurements in propulsion applications. Furthermore, multiple identical devices could be deployed (at least 2) in the circumference of the shaft without requiring additional space in the volume swept by the VEH, thus improving the achieved power density without breaching potential space constraints. The power density could be further improved by minimising the necessary structure that supports the harvesting parts; yet the focus of this paper is on the experimental demonstration of the self-tuned VEH concept, and therefore, any Research and Development advancements

**Table 2**
Performance comparison to VEH devices in the literature.

| References | Conversion Mechanism | Device Dimension | Input Excitation | Self-tuning & Nonlinearity | Bandwidth [Hz] | Peak Power |
|---|---|---|---|---|---|---|
| Gu & Livermore 2010 [9] | Piezoelectric | $80 \times 5 \times 0.45$ mm | Continuous rotation | Centrifugal force | 5 to 20 | 0.7 mW |
| Hsu et al. 2014 [10] | Piezoelectric | $85 \times 18 \times 0.4$ mm | Continuous rotation | Centrifugal force | 15 to 30 | 1.5 mW |
| Fu & Yeatman 2019 [24] | Piezoelectric | $34 \times 2 \times 0.15$ mm | Continuous rotation | Bi-stability | 4 to 11 | 50 μW |
| Mei et al. 2021 [34] | Piezoelectric | $80 \times 12 \times 0.2$ mm | Continuous rotation | Multi-stable Centrifugal | 7 to 10 | N/A |
| This work | Electromagnetic | $60 \times 20 \times 20$ mm | Rotational oscillation | Tautochrone oscillation | 10 to 35 | 4 mW |
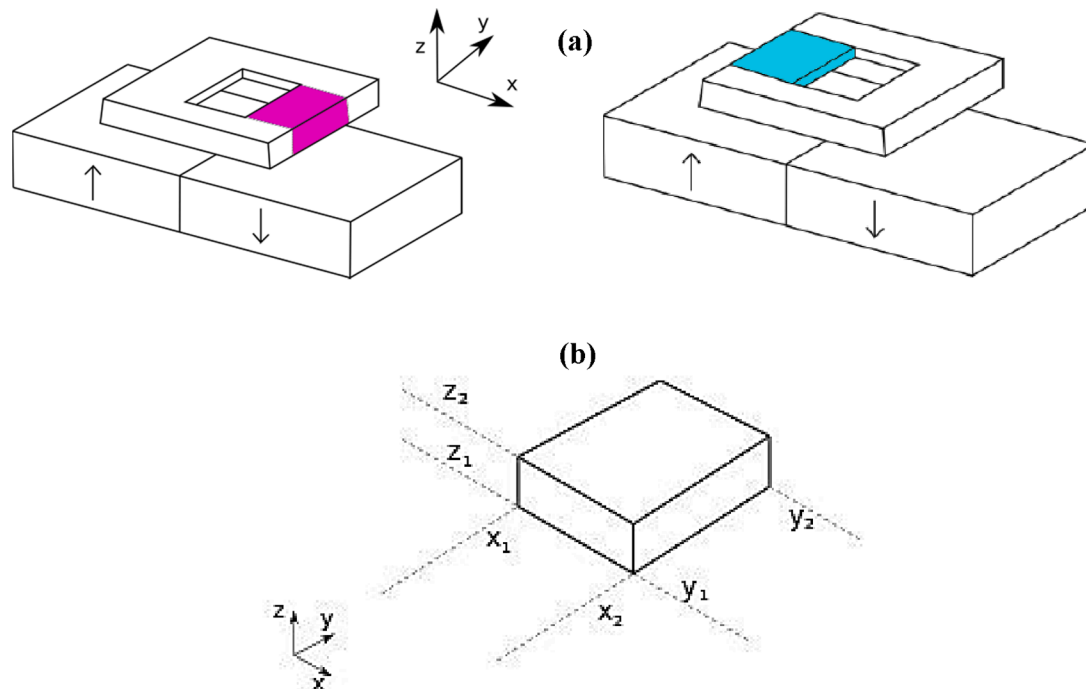


**Fig. A1.** (a) First (left) and second (right) section of the coil and (b) Magnet boundaries.

are beyond the scope of the presented study.

### 4.4. Comparison to rotational VEH devices presented in the literature

Table 2 provides the comparison of the rotational VEH device in this work to the existing ones in the literature. The adopted mechanism, device dimension, input excitation, self-tuning and nonlinear mechanisms, operation bandwidth and the peak output power are summarized. The beam-based piezoelectric energy harvesters are the typical self-tuned rotational VEH solution combined with the associated centrifugal force [9]. Nonlinear operation, such as bi-stability [24], is another way to enhance the operational bandwidth. From Table 2, it is worth noting that electromagnetic conversion is less studied in self-tuned energy harvesting devices, which also illustrates the novelty of this work. The 'tautochrone' path combined with an eccentric mass for self-tuning in energy harvesting is presented in this work for the first time, to the best of the authors' knowledge. The high power output with the wide operation bandwidth demonstrates the potential of this type of energy harvester for powertrain monitoring.

### 5. Conclusions and future work

A self-tuned, rotational vibration energy harvester for powering wireless sensors in powertrains has been presented in this work. An electro-mechanical numerical model of the vibration energy harvester has been developed and was validated by a physical prototype that was tested in a laboratory powertrain rig. The test rig was driven by an electric motor with rotational speed fluctuations induced by a universal joint. The model was shown to accurately predict the performance of the vibration energy harvester both in terms of mechanical vibration and electrical voltage data.

The vibration energy harvester is self-tuned to a selected multiple of the powertrain shaft rotational speed. The implementation of such a compact design enables greater amounts of energy to be harvested across the operating range of the shaft speed. The concept differs from those previously reported in the literature in that it makes no use of protruding beams, allowing for fitment in small spaces around shafts.

The vibration energy harvester has been experimentally proven to work in a robust manner across shaft rotational speeds between 500 and 2000 rpm. Below 1200 rpm, insufficient power was generated to charge the load capacitor in the present configuration but future optimisation of the vibration energy harvester could allow for higher power generation in the low speed range as well. The vibration energy harvester power output could also be increased simply by adding more pendulums around the circumference of the shaft without any significant penalty in terms of the swept volume.

The future work should focus on optimising the electromechanical coupling of the vibration energy harvester to achieve higher power output at a broader speed range of interest (up to 10,000 rpm). The effect of impacts of the pendulum mass (when reaching the ends of the curved tracks) on the vibration energy harvester durability and performance should be studied. The addition of more pendulums tuned to operate in phase difference should also be studied in combination to the system stability properties. Once these objectives have been achieved, experimental testing in real world applications (propulsion systems) should be pursued.

## CRediT authorship contribution statement

**B. Gunn:** Visualization, Writing - original draft, Investigation, Formal analysis, Software, Validation, Methodology, Conceptualization. **P. Alevras:** Writing - review & editing, Investigation, Validation. **J.A. Flint:** Funding acquisition, Writing - review & editing, Investigation, Validation. **H. Fu:** Writing - review & editing, Validation. **S.J. Rothberg:** Methodology, Conceptualization. **S. Theodossiades:** Funding acquisition, Supervision, Writing - review & editing, Investigation, Project administration, Methodology, Conceptualization.

## Declaration of Competing Interest

The authors declare that they have no known competing financial interests or personal relationships that could have appeared to influence the work reported in this paper.

## Appendix

This Appendix gives the derivation of the electromagnetic coupling factor, $\widehat{\Theta}$, introduced in equation (12).

The Lorentz force law gives the force exerted on a current-carrying conductor in an external magnetic field [31]. The infinitesimal force, $d\mathbf{F}$ acting on an infinitesimal length of wire, $d\mathbf{l}$ is found by multiplying the flowing current by the cross product of the infinitesimal length and the magnetic flux density, $\mathbf{B}$, at that point [31]:

$$d\mathbf{F} = i\, d\mathbf{l} \times \mathbf{B} \quad (A1)$$

where $i$ denotes electrical current flowing through a conductor and $\mathbf{B}$ is the magnetic flux density at a point away from the magnet. Bold type denotes a vector.

The coil of wire is considered in four sections. Fig. A1 (a) shows the first and second sections to be considered aligned across the y-direction and highlighted. The datum in the top right of the figure shows the x, y and z directions as referred to throughout this Appendix.

In the first section, the wire is aligned with the y axis. Thus, equation (A1) becomes:

$$\begin{bmatrix} dF_x \\ dF_y \\ dF_z \end{bmatrix} = i \begin{bmatrix} 0 \\ dl_y \\ 0 \end{bmatrix} \times \begin{bmatrix} B_x \\ B_y \\ B_z \end{bmatrix} \quad (A2)$$

Evaluating the cross product and integrating gives:

$$\begin{bmatrix} F_x \\ F_y \\ F_z \end{bmatrix} = i \begin{bmatrix} -\int B_z dl_y \\ 0 \\ \int B_x dl_y \end{bmatrix} \quad (A3)$$

Projecting the force on the direction of motion for the first and second sections gives:

$$F_s = i \begin{bmatrix} -\int B_z dl_y \\ 0 \\ \int B_x dl_y \end{bmatrix} \cdot \begin{bmatrix} \cos(\theta) \\ 0 \\ -\sin(\theta) \end{bmatrix} \quad (A4)$$

which yields:

$$F_s = -i\left(\int B_z dl_y \cos(\theta) + \int B_x dl_y \sin(\theta)\right) \quad (A5)$$

Defining the expression in the integrals as the coupling factor per turn:

$$\widehat{\Theta}_{turn} = -\left(\int B_z dly \cos(\theta) + \int B_x dly \sin(\theta)\right) \quad (A5)$$

A similar procedure can be followed for the coil sections aligned across the x-direction in Fig. A1 (a). However, the wire length in these sections is significantly shorter than in the sections aligned with the y-axis, and the only contribution comes from the y component of the field which is negligible in comparison to the x and z components. Therefore, the effects of electromagnetic induction in the other sections will be neglected from now on.

To obtain the per-turn average coupling factor of the coil, Eq. (A5) is integrated with respect to the coil width and coil depth and then divided by the cross sectional area of the conductor in the coil to get the average coupling factor over the whole coil:

$$\widehat{\Theta}_{mean} = \frac{1}{w_c d_c} \int_{w_c} \int_{d_c} \widehat{\Theta}_{turn}\, dw_c\, dd_c \quad (A6)$$

The total coupling factor of the whole coil can be found by multiplying by the total number of coils:

$$\widehat{\Theta} = N_c \widehat{\Theta}_{mean} \quad (A7)$$

To find the coupling factor, an equation for the field is now required. Fig. A1 (b) shows a schematic of the boundaries of an isolated magnet in free space.

$B_x$ is found by numerical evaluation of the following 3D field equations [31]:

$$B_x(x,y,z) = \frac{\mu_0 M_s}{4\pi} \sum_{k=1}^{2} \sum_{m=1}^{2} (-1)^{k+m} \ln[F(x,y,z,x_m,y_1,y_2,z_k)] \tag{A8}$$

where $F(x,y,z,x_m,y_1,y_2,z_k)$ is given by:

$$F(x,y,z,x_m,y_1,y_2,z_k) = \frac{(y-y_1) + [(x-x_m)^2 + (y-y_1)^2 + (z-z_k)^2]^{1/2}}{(y-y_2) + [(x-x_m)^2 + (y-y_2)^2 + (z-z_k)^2]^{1/2}} \tag{A9}$$

and $B_z$ is given by:

$$B_z(x,y,z) = \frac{\mu_0 M_s}{4\pi} \sum_{k=1}^{2} \sum_{m=1}^{2} \sum_{n=1}^{2} (-1)^{k+m+n} \arctan\left[\frac{(x-x_n)(y-y_m)}{(z-z_k)} g(x,y,z;x_n,y_m,z_k)\right] \tag{A10}$$

where $g(x,y,z;x_n,y_m,z_k)$ is given by:

$$g(x,y,z;x_n,y_m,z_k) = \frac{1}{[(x-x_n)^2 + (y-y_m)^2 + (z-z_k)^2]^{1/2}} \tag{A11}$$

where $(x,y,z)$ is the infinitesimal point on the coil that is of interest and $x_n$, $y_m$ and $z_k$ define the boundaries of the magnet as depicted in Fig. A1 (b). Combination of Eq. (A7) – A(11) gives the final expression for the electromagnetic coupling factor which is used in this paper.

# References

[1] Khazaee M, Rezaniakolaie A, Moosavian A, Rosendahl L. A novel method for autonomous remote condition monitoring of rotating machines using piezoelectric energy harvesting approach. Sens Actuators A Phys 2019;295:37–50.

[2] Tang Q, He Q, Li M, Dong C, Xu D, Li X. Wireless Alarm Microsystem Self-Powered by Vibration-Threshold-Triggered Energy Harvester. IEEE Trans Ind Electron 2016; 63(4):2447–56. https://doi.org/10.1109/TIE.2015.2510503.

[3] Liu H, et al. Hybrid energy harvesting technology: From materials, structural design, system integration to applications. Renew Sustain Energy Rev 2020.

[4] Gholikhani M, et al. A critical review of roadway energy harvesting technologies. Appl Energy 2020;261.

[5] Elliott, A., et al. Which is better, electrostatic or piezoelectric energy harvesting systems? in Journal of Physics: Conference Series. 2015. IOP Publishing.

[6] Moss SD, et al. Scaling and power density metrics of electromagnetic vibration energy harvesting devices. Smart Mater Struct 2015;24(2).

[7] Carneiro P, et al. Electromagnetic energy harvesting using magnetic levitation architectures: A review. Appl Energy 2020;260.

[8] Nguyen HT, Genov DA, Bardaweel H. Vibration energy harvesting using magnetic spring based nonlinear oscillators: Design strategies and insights. Appl Energy 2020;269.

[9] Gu L, Livermore C. Passive self-tuning energy harvester for extracting energy from rotational motion. Appl Phys Lett 2010;97(8).

[10] Hsu J-C, Tseng C-T, Chen Y-S. Analysis and experiment of self-frequency-tuning piezoelectric energy harvesters for rotational motion. Smart Mater Struct 2014;23 (7).

[11] Roundy S, Tola J. An energy harvester for rotating environments using offset pendulum dynamics. IEEE; 2013.

[12] Maurya D, et al. Energy harvesting and strain sensing in smart tire for next generation autonomous vehicles. Appl Energy 2018;232:312–22.

[13] Pillatsch P, Yeatman EM, Holmes AS. A piezoelectric frequency up-converting energy harvester with rotating proof mass for human body applications. Sens Actuators, A 2014;206:178–85.

[14] Izadgoshasb I, et al. Improving efficiency of piezoelectric based energy harvesting from human motions using double pendulum system. Energy Convers Manage 2019;184:559–70.

[15] Toh TT, et al. A continuously rotating energy harvester with maximum power point tracking. J Micromech Microeng 2008;18(10).

[16] Fu H, et al. Ultra-low frequency energy harvesting using bi-stability and rotary-translational motion in a magnet-tethered oscillator. Nonlinear Dyn 2020;101(4): 2131–43.

[17] Trimble AZ, et al. A device for harvesting energy from rotational vibrations. J Mech Des 2010;132(9).

[18] Musgrave, P., W. Zhou, and L. Zuo. Piezoelectric energy harvesting from torsional vibration. in International Design Engineering Technical Conferences and Computers and Information in Engineering Conference. 2015. American Society of Mechanical Engineers.

[19] Qian F, et al. Theoretical modeling and experimental validation of a torsional piezoelectric vibration energy harvesting system. Smart Mater Struct 2018;27(4).

[20] Gunn, B., P. Alevras, and S. Theodossiades. Energy harvesting from torsional vibrations using a nonlinear oscillator. in International Design Engineering Technical Conferences and Computers and Information in Engineering Conference. 2016. American Society of Mechanical Engineers.

[21] Alevras P, Theodossiades S, Rahnejat H. On the dynamics of a nonlinear energy harvester with multiple resonant zones. Nonlinear Dyn 2018;92(3):1271–86.

[22] Gunn B, Theodossiades S, Rothberg S. A nonlinear concept of electromagnetic energy harvester for rotational applications. J Vib Acoust 2019;141(3).

[23] Gao M, et al. Experimental investigation of non-linear multi-stable electromagnetic-induction energy harvesting mechanism by magnetic levitation oscillation. Appl Energy 2018;220:856–75.

[24] Fu, H. and E.M. Yeatman, Rotational energy harvesting using bi-stability and frequency up-conversion for low-power sensing applications: Theoretical modelling and experimental validation. Mechanical Systems and Signal Processing, 2019. 125: p. 229-244.

[25] Chao, C.-P., S. Shaw, and C.-T. Lee, Stability of the unison response for a rotating system with multiple tautochronic pendulum vibration absorbers. 1997.

[26] Kim G. Piezoelectric energy harvesting from torsional vibration in internal combustion engines. Int J Automot Technol 2015;16(4):645–51.

[27] Alevras P, Theodossiades S. Vibration energy harvester for variable speed rotor applications using passively self-tuned beams. J Sound Vib 2019;444:176–96.

[28] Denman H. Tautochronic bifilar pendulum torsion absorbers for reciprocating engines. J Sound Vib 1992;159(2):251–77.

[29] Hibbeler, R.C. and R.C. Hibbeler, Engineering mechanics: statics & dynamics. 2007: Pearson Education India.

[30] Contact properties. Available from: http://atc.sjf.stuba.sk/files/mechanika_vms_ ADAMS/Contact_Table.pdf.

[31] Furlani, E.P., Permanent magnet and electromechanical devices: materials, analysis, and applications. 2001: Academic press.

[32] Schmelz, F., H.C. Seherr-Thoss, and E. Aucktor, Universal joints and driveshafts: analysis, design, applications. 1992: Springer.

[33] Wireless MCU. Available from: http://www.ti.com/lit/ds/symlink/cc2650.pdf.

[34] Mei X, et al. A passively self-tuning nonlinear energy harvester in rotational motion: theoretical and experimental investigation. Smart Mater Struct 2020;29 (4).